Theoretical insight into Ar–O_2 surface-wave microwave discharges

2010 J. Phys. D: Appl. Phys. 43 175201

(http://iopscience.iop.org/0022-3727/43/17/175201)

J. Phys. D: Appl. Phys. **43** (2010) 175201 (14pp) doi:10.1088/0022-3727/43/17/175201

Theoretical insight into Ar–O_2 surface-wave microwave discharges

Kinga Kutasi[1], **Vasco Guerra**[2] **and Paulo Sá**[2,3]

[1] Research Institute for Solid State Physics and Optics, Hungarian Academy of Sciences, POB 49, H-1525 Budapest, Hungary
[2] Instituto de Plasmas e Fusão Nuclear, Instituto Superior Técnico, 1049-001 Lisboa, Portugal
[3] Departamento de Engenharia Física, Faculdade de Engenharia da Universidade do Porto, 4200-465 Porto, Portugal

E-mail: kutasi@sunserv.kfki.hu

Received 23 November 2009, in final form 10 March 2010
Published 15 April 2010
Online at stacks.iop.org/JPhysD/43/175201

Abstract
A zero-dimensional kinetic model has been developed to investigate the coupled electron and heavy-particle kinetics in Ar–O_2 surface-wave microwave discharges generated in long cylindrical tubes, such as those launched with a surfatron or a surfaguide. The model has been validated by comparing the calculated electron temperature and species densities with experimental data available in the literature for different discharge conditions. Systematic studies have been carried out for a surface-wave discharge generated with 2.45 GHz field frequency in a 1 cm diameter quartz tube in Ar–O_2 mixture at 0.5–3 Torr pressures, which are typical conditions found in different applications. The calculations have been performed for the critical electron density for surface-wave propagation, $n_e = 3.74 \times 10^{11}$ cm^{-3}.
It has been found that the sustaining electric field decreases with Ar percentage in the mixture, while the electron kinetic temperature exhibits a minimum at about 80%Ar. The charged and neutral species densities have been calculated for different mixture compositions, from pure O_2 to pure Ar, and their creation and destruction processes have been identified. The O_2 dissociation degree increases with Ar addition into O_2 and dissociation degrees as high as 60% can be achieved. Furthermore, it has been demonstrated that the dissociation degree increases with the discharge tube radius, but decreases with the atomic surface recombination of O-atoms. The density of O^- negative ions is very high in the plasma, the electronegativity of the discharge can be higher than 1, depending on the discharge conditions.

1. Introduction

Oxygen containing discharges and their afterglows have a wide range of applications due to the presence of active O(^{3}P) and O(^{1}D) atoms [1–3], excited $O_2(a\,^1\Delta_g)$ molecules [4–7] and the ground state $O_2(X\,^3\Sigma_g^-, v)$, which together with Ar^+ have been proven to be able to inactivate bacteria spores [8]. O_2 and Ar–O_2 plasmas have been successfully used for oxide films deposition [9, 10], synthesis of metal oxide nanowires [11], sterilization and decontamination of medical instruments [1, 12–15] and polymer surface treatment [3, 16–18]. Furthermore, the O(^{1}D) atoms present in Ar–O_2 plasma were shown to have the potential for surface activation [2].

The O_2 and Ar–O_2 surface-wave microwave discharges and post-discharges used for different applications have been experimentally investigated by numerous groups with the aim of determining the density of active species in the processing zone. The O-atoms density was determined in the post-discharge of an Ar–O_2 surface-wave microwave discharge by titration by Ricard *et al* [19–21] and Belmonte *et al* [22], for selected discharge conditions and mixture composition. Recently, two further techniques have been developed for the measurement of O-atoms density, one spectroscopical diagnostic that is based on the emission spectra of the $O_2(b\,^1\Sigma_g^+, v = 0 \rightarrow X\,^3\Sigma_g^-, v' = 0)$ transition [3, 18] and one probe method that relies on the temperature rise of a catalytic probe due to the atomic recombination on the probe

surface [23, 24]. For the case of a pure O_2 surface-wave microwave discharge the O-atoms density was obtained by VUV absorption spectroscopy downstream of the discharge by Granier *et al* [25] for different discharge configurations and microwave frequencies.

Clearly, experimental measurements can provide very important information regarding the composition of the discharge, as revealed by the above-mentioned works. However, a more complete picture of the complex discharge can be obtained by complementary modelling techniques. Discharge models significantly contribute to the understanding of the elementary processes occurring in the plasma. As a matter of fact, besides the density of oxygen atoms and excited molecules, they can give the density of all the species present in the discharge and its afterglow, as well as provide all details about the electron and heavy-particle kinetics. Previous theoretical investigations carried out on surface-wave microwave discharges generated with the help of a surfatron focused mostly on pure O_2 [25–28] and Ar [29, 30] discharges, but a detailed study of the Ar–O_2 mixture is still missing at present. Ar–O_2 plasmas have been investigated in more detail in the case of capacitively coupled plasmas (CCPs) [31, 32] and inductively coupled plasmas (ICPs) [33, 34] operating at lower pressures in the milliTorr regime with a rather different electron and molecular kinetics.

The purpose of this work is to develop a self-consistent kinetic model that allows the description of the Ar–O_2 surface-wave microwave discharges generated in long cylindrical tubes, such as those launched with a surfatron or surfaguide. Moreover, the model is systematically used as a tool to acquire physical insight into the kinetics and the basic properties of the discharge. The primary system under analysis is a discharge operating at low pressures, $p = 0.5$–2 Torr, generated with a field frequency of $\omega/2\pi = 2.45$ GHz in a quartz tube with inner radius $R = 0.5$ cm, for an electron density equal to the critical density for surface-wave propagation, $n_e = n_{ec} = 3.74 \times 10^{11}$ cm^{-3}. The gas temperature is chosen to be 1000 K [26, 35, 36]. These conditions are close to the typical discharge conditions determining the afterglows used in the experimental plasma sterilization [1, 21] and polymer treatment studies [3]. Other conditions will be additionally investigated, in order to better validate the model and to elucidate the role of heterogeneous processes.

2. Model description

Surface-wave microwave discharges in long cylindrical tubes at low gas flows can be described with a zero-dimensional kinetic model that is based on the homogeneous electron Boltzmann equation, coupled together with the rate balance equations describing the creation and destruction of the most important neutral and charged particles. Clearly a zero-dimensional model solves at each step a given cross section of the discharge tube, but the axial structure can nevertheless be obtained from the additional coupling of the wave-to-plasma power balance equation for the electron density gradient, as detailed in [37]. Herein we do not address the axial structure of the discharge, since we are essentially interested in the region close to the end of the discharge, defining the conditions for the afterglow. Accordingly, the discharge model is used for the critical electron density for surface-wave propagation.

The steady-state, homogeneous electron Boltzmann equation is solved in an Ar–O_2–O mixture, using the 2-term expansion in spherical harmonics. It takes into account the elastic collisions, electron–electron collisions, superelastic collisions producing electronic deexcitation from the usually populated states $O_2(a\,^1\Delta_g)$ and $O_2(b\,^1\Sigma_g^+)$, as well as the transitions between these latter two states induced by electron impact. The present model also includes, in parallel with electron dissociation and ionization of $O_2(X)$, electron impact dissociation of $O_2(a)$ and $O_2(b)$ and electron stepwise ionization from $O_2(a)$. Additionally, excitation and ionization from ground state O(^{3}P) and Ar(^{1}S$_0$) atoms, as well as the excitation and ionization from the excited Ar(4s) states, are also considered. The mathematical techniques used for solving the Boltzmann equation for the case of a microwave field can be found in [38, 39]. The field frequency ω is assumed to be sufficiently high so that the electrons do not lose appreciable energy during a cycle of field oscillation and the electron energy distribution function (EEDF) can be assumed stationary. Note that the term of energy gain due to the electric field depends on the ratio $E^2/(\nu_c^2 + \omega^2)$, where ν_c is the electron–neutral collision frequency (which is a function of the electron energy) and $E = E_0/\sqrt{2}$ is the rms field, E_0 denoting the field amplitude [38, 39].

The reduced sustaining microwave field (E/N) for the plasma in a cylindrical tube is self-consistently calculated in the model. The continuity and transport equations for the electrons, different positive ions and O^- ions are solved, in order to describe the charged particle motion to the wall under the presence of the radial space-charge field. The reduced electric field is determined using the requirement that under steady-state conditions the total rate of ionization must compensate exactly for the rate of electron loss by coupled diffusion to the wall plus electron–ion recombination. The rates of electron attachment to O_2 molecules and electron detachment from O^- also constitute loss and gain terms, respectively, in the rate balance equation for electrons. Furthermore, the presence of negative ions modifies the charged particles' radial profiles, with a corresponding modification of their diffusion characteristics. This effect is taken into account as detailed in [40].

A surface-wave microwave discharge is a plasma column with a decreasing electron density profile. At the end of the plasma column the electron density reaches the value of the critical density for surface-wave mode propagation in a homogeneous, cold, collisionless plasma, surrounded by a dielectric of permittivity ϵ_g. The surface-wave mode can only propagate provided the electron density is larger than this critical value, obtained from $\omega_{pe} > \omega\sqrt{1+\epsilon_g}$, with ω_{pe} denoting the electron plasma angular frequency, which for a quartz tube ($\epsilon_g = 4$) gives $n_{ec} = 3.74 \times 10^{11}$ cm^{-3} at 2450 MHz. Our calculations are conducted for this critical electron density, so that the discharge characteristics, as well as the species densities, are obtained at the end of the plasma column. Therefore, they can be used as initial values for

Table 1. Collisional and radiative processes for argon species as considered in the model. The rate coefficients of different processes are taken from [42, 43] or calculated as described in [42] and references therein. s_j denotes the four levels of $3p^5 4s$ state: two metastable $^3P_0$, $^3P_2$ and two resonant $^3P_1$,$^1P_1$.

R1	$Ar(^1S_0) + e \rightarrow Ar(4s_j) + e$
R2	$Ar(^1S_0) + e \rightarrow Ar^* + e$
R3	$Ar^* \rightarrow ... \rightarrow Ar(4s_j) + h\nu$
R4	$Ar(4s_j) + e \rightarrow Ar(4s_i) + e$
R5	$Ar(4s_j) + e \rightarrow Ar(4p) + e$
R6	$Ar(4p) \rightarrow Ar(4s_j) + h\nu$
R7	$Ar(4s_j) \rightleftarrows Ar(^1S_0) + h\nu$
R8	$Ar(4s_j) + wall \rightarrow Ar(^1S_0)$
R9	$Ar(4s_j) + e \rightarrow Ar(^1S_0) + e$
R10	$Ar(4s_j) + e \rightarrow Ar^+ + 2e$
R11	$Ar(4s_j) + Ar(4s_i) \rightarrow Ar(^1S_0) + Ar^+ + e$
R12	$e + Ar(^1S_0) \rightarrow e + e + Ar^+$
R13	$Ar^+ + Ar(^1S_0) + Ar(^1S_0) \rightarrow Ar_2^+ + Ar(^1S_0)$
R14	$Ar_2^+ + e \rightarrow Ar(4p) + Ar(^1S_0)$

afterglow studies, since most of the applications rely on the early- or late-afterglow (present in a large volume reactor) of the flowing surface-wave discharge [3, 20, 23, 41]. Take note that an axial description of a surface-wave discharge can be achieved by coupling the wave and the electron power equations. Such an axial description goes beyond the purpose of the present research, but all details on how to do it can be found in [37], where a study of the axial structure of a surface-wave nitrogen discharge was conducted.

In what concerns the heavy-particle kinetics the model solves the rate balance equations for the following argon and oxygen species: $Ar(^1S_0, {}^3P_2, {}^3P_1, {}^3P_0, {}^1P_1)$, $O_2(X\,{}^3\Sigma_g^-, v)$, $O_2(a\,{}^1\Delta_g, b\,{}^1\Sigma_g^+)$, $O(^3P, {}^1D)$, O_3, Ar^+, Ar_2^+, O_2^+, O^+ and O^-. The collisional–radiative module that describes the excitation and deexcitation of the $3p^5 4s$ levels in a pure Ar discharge has been developed according to the collisional–radiative model of Ferreira *et al* [29, 42]. A list of the Ar collisional and radiative processes taken into account is given in table 1. With O_2 addition to Ar further collisional processes are included, as listed in table 2, which play an important role in the determination of the Ar ground state, metastable and resonant states populations and oxygen dissociation degree. The gas reactions that govern the density of oxygen species as considered in the model are presented in table 3.

Besides the gas-phase reactions, a crucial role is also played by the surface reactions, such as heterogeneous recombination of O atoms. The recombination of O atoms on surfaces strongly depends on the surface temperature, a sharp increase in the surface recombination probability (γ) with temperature was observed above 300 K by Macko *et al* [56] for a pyrex surface exposed to an oxygen dc discharge. In the case of air-cooled surfatron generated surface-wave discharges, tube surface temperatures of about 400 K can be expected. Accordingly, using the results of [56] we have chosen $\gamma_{O(^3P)} = 10^{-2}$. Furthermore, the wall deactivation probabilities of $O(^1D)$, $O_2(a)$ and $O_2(b)$ were taken to be 1, 2×10^{-5} and 2×10^{-2}, respectively [26, 55].

The wall loss process of species is considered as in [57, 58], with a characteristic time τ_i, given by

$$\tau_i = \frac{1}{D_i}\left(\frac{R}{2.405}\right)^2 + \frac{2R(1-\gamma_i/2)}{\gamma_i \langle v_i \rangle}, \qquad (1)$$

where i denotes the different species, D_i is the diffusion coefficient of species i in the mixture, $\langle v_i \rangle$ its thermal speed and γ_i its destruction probability at the wall. Note that $\tau_i^{-1} \simeq \gamma_i \langle v_i \rangle / 2R$ when $\gamma_i \ll 1$ and $\tau_i^{-1} \simeq D_i (2.405/R)^2$ in the limit $\gamma_i \rightarrow 1$.

The diffusion coefficients D_i of species i in the mixture were calculated from the simplified Wilke's formula, as given in [59],

$$D_i = \frac{1 - x_i}{\sum_{i \neq j} \frac{x_j}{D_{ij}}}. \qquad (2)$$

In this expression x_i is the relative concentration of species i and D_{ij} are the binary diffusion coefficients of species i and j, given by Hirschfelder [60] as

$$D_{ij}(\mathrm{cm^2\,s^{-1}}) = \frac{1.929 \times 10^{19} \sqrt{\frac{T[K]}{2\mu}}}{N(\mathrm{cm^{-3}})\sigma_{12}^2[\mathrm{\AA^2}]\Omega^{(1,1)*}(T^*)}, \qquad (3)$$

where μ denotes the reduced mass, $T^* = kT/\varepsilon_{12}$, σ_{12} and ε_{12} are parameters of the Lennard-Jones interaction potential. The collision integral $\Omega^{(1,1)*}$ is tabulated in [60], while the binary potential parameters in equation (3) are obtained from $\varepsilon_{ij} = \sqrt{\varepsilon_i \varepsilon_j}$ and $\sigma_{ij} = (\sigma_i + \sigma_j)/2$. In practice all species are considered to diffuse in an Ar–O_2–O mixture, where we have taken $\varepsilon(O)/k = 124\,K$, $\varepsilon(O_2)/k = 113\,K$ and $\varepsilon(O)/k = 124\,K$, whereas $\sigma(Ar) = 3.42\,\mathrm{\AA}$, $\sigma(O_2) = 3.43\,\mathrm{\AA}$ and $\sigma(O) = 2.60\,\mathrm{\AA}$. The binary diffusion coefficients are calculated from (3), but renormalized whenever possible to fit the data reported in [10, 42, 61–63]. The values of the binary diffusion coefficients used are given for $p = 1$ Torr and $T = 273$ K in table 4.

Under the formulation presented here, the model provides the species densities, the electric field sustaining the discharge, the electron energy distribution function (EEDF) and all the information concerning the electron excitation rate coefficients and transport parameters, as well as all the details concerning the chemical kinetics of each species.

The model was developed with the aim of studying discharges operating at pressures of around 1 Torr in tubes with an inner ratio of the order of 1 cm. Its validity for these conditions is established in the next section. Nevertheless, it is interesting to estimate the range of parameters, in particular the gas temperature, T_g, pressure, p, and reduced electric field, E/N, for which the model is applicable.

The limitation due to the gas temperature arises only from the temperature dependence of the heavy-particle rate coefficients, as several of them were measured and validated either at room temperature or within a limited range of T_g. We estimate that our rate coefficients may give reliable results up to ~1500 K. For higher gas temperatures, a careful revision of the reaction rate coefficients is required.

A change in pressure, assuming the remaining parameters to be the same, does not introduce any major difficulty.

Table 2. Collisional and radiative processes between argon and oxygen species. The rate coefficients for the two- and three-body reactions are in $cm^3\ s^{-1}$ and $cm^6\ s^{-1}$, respectively, and the decay frequencies are in s^{-1}.

Processes		Rate coefficients	References
R15	$Ar(4s_j) + O_2(X, 0) \rightarrow Ar(^1S_0) + O(^3P) + O(^3P)$	$0.46 \times 2.1 \times 10^{-10}$ [a]	[44, 45]
R16	$Ar(4s_j) + O_2(X, 0) \rightarrow Ar(^1S_0) + O(^3P) + O(^1D)$	$0.52 \times 2.1 \times 10^{-10}$ [a]	[44, 45]
R17	$Ar(4s_j) + O \rightarrow Ar(^1S_0) + O$	4.1×10^{-11}	[32]
R18	$O^- + Ar^+ \rightarrow Ar(^1S_0) + O(^3P)$	2.8×10^{-7}	[33, 46]
R19	$Ar(^1S_0) + O_2(X, 0) + O(^3P) \rightarrow Ar(^1S_0) + O_3$	$3.9 \times 10^{-34} \times (300/T)^{1.9}$	[10]
R20	$Ar(^1S_0) + O(^3P) + O(^3P) \rightarrow Ar(^1S_0) + O_2(X, 0)$	$5.2 \times 10^{-35} \times \exp(900/T)$	[10]
R21	$Ar(^1S_0) + O_2(b) \rightarrow Ar(^1S_0) + O_2(X, 0)$	1.5×10^{-17}	[10, 47]
R22	$Ar(^1S_0) + O(^1D) \rightarrow Ar(^1S_0) + O(^3P)$	3×10^{-13}	[10, 33]
R23	$O(^3P) + Ar^+ \rightarrow Ar(^1S_0) + O^+$	6.4×10^{-12}	[33]
R24	$O_2 + Ar^+ \rightarrow Ar(^1S_0) + O_2^+$	$4.9 \times 10^{-11} \times (300/T)^{0.78}$ $+9.2 \times 10^{-10} \times \exp(-5027.6/T)$	[48]

[a] 2.4 instead of 2.1 for the $Ar(^3P_0)$ state.

Moving to higher pressure may just call for the inclusion of a few additional three-body reactions in the kinetic scheme. However, changing the pressure entails modifications in the self-consistent values of the electric field, which impose much more severe restrictions. On the one hand, at low pressure the electric field increases, and the validity of the two-term approximation in the electron Boltzmann equation becomes questionable; as a rule of thumb, one should start worrying if the *reduced effective field* [38, 39] goes above ~200 Td (for a tube radius of 0.5 cm this means we cannot go much lower in pressure than the 0.5 Torr used in some calculations in the next section). On the other hand, at higher pressures the reduced effective field may become too small for the electron energy discretization we use (in steps of 0.1 eV). In either case the structure of the model can remain the same, but we would have to modify and improve our Boltzmann solver. In some situations the use of a Maxwellian distribution may be justified, allowing the straightforward use of the present model in extreme situations.

3. Results and discussion

This section starts by establishing the overall correctness and predictive power of our model. To this purpose, we compare our calculations with some of the few available experimental measurements for surfatron generated discharges in relatively well-defined conditions, close to the ones of interest in this study. Once this benchmarking is accomplished, we proceed to a detailed analysis of the different kinetics and to the investigation of the elementary processes occurring in the discharge.

3.1. Validation of the model

In order to substantiate the validity of the model, different experimental systems have been modelled, including surface-wave discharges generated in each of the pure gases and also in the Ar–O_2 mixture. First, we have chosen the surface-wave discharge system experimentally studied by Granier *et al* [25]. There, an oxygen discharge was generated in a 1.6 cm diameter quartz tube at 1 Torr and at a frequency of 390 MHz, corresponding to a critical electron density of $9.46 \times 10^9\ cm^{-3}$. Granier *et al* have measured the $O(^3P)$ oxygen atomic concentration as well as the $O_2(a\ ^1\Delta_g)$ singlet oxygen concentration. According to their measurements the discharge gas temperature under these conditions is 420 K, resulting in a total gas density of $2.3 \times 10^{16}\ cm^{-3}$. Due to this low gas temperature, much lower than that measured in the case of 2.45 GHz generated discharges, the surface temperature also becomes lower. As a consequence, in compliance with Macko *et al* [56], the atomic surface recombination coefficient is lower than in the case of the 2.45 GHz generated discharges, 8×10^{-3} compared with 10^{-2}. According to figures 6 and 8 from [25], the measured $O_2(X\ ^3\Sigma_g^+)$, $O_2(a\ ^1\Delta_g)$ and $O(^3P)$ densities are $2.1 \times 10^{16}\ cm^{-3}$, $2 \times 10^{15}\ cm^{-3}$ and $10^{15}\ cm^{-3}$, respectively. From the experimentally determined densities, the dissociation degree, defined as $[O]/2[O_2]$, is about 2.17%. Our calculations conducted for the same discharge conditions yield $[O_2(X)] = 1.97 \times 10^{16}\ cm^{-3}$, $[O_2(a)] = 2.4 \times 10^{15}\ cm^{-3}$ and $[O(^3P)] = 9.99 \times 10^{14}\ cm^{-3}$, corresponding to a dissociation degree of 2.17%, in perfect agreement with the experimentally determined values. Furthermore, a quasi-perfect match with the experimentally measured $O_2(a)$ density is obtained, $1.98 \times 10^{15}\ cm^{-3}$, if the wall deactivation probability of $O_2(a)$ is increased from 2×10^{-5} to 5×10^{-4}.

As a next step we compare our simulations with the experimental results obtained by de Vries *et al* [64] in an Ar surface-wave discharge generated at 2.45 GHz, in a quartz tube with inner radius 0.3 cm. In [64] electron density and temperature measurements are reported for different pressures, ranging from 4.5 to 15 Torr. For the two extreme pressure values, $p = 4.5$ and 15 Torr, the experimentally determined electron densities (n_e) are $2.1 \times 10^{13}\ cm^{-3}$ and $4.1 \times 10^{13}\ cm^{-3}$, respectively, while the corresponding electron temperatures (T_e) are 1.24 eV and 1.16 eV, respectively. The errors indicated by the authors are about 8% for both n_e and T_e, and further, in the case of n_e an additional systematic error of 8% is also mentioned. We have conducted calculations for these two pressure values by using in the model the experimentally determined electron densities given above. The electron temperatures obtained in this way are $T_e = 1.51$ and 1.24 eV, respectively, which reflect the correct pressure dependence and, taking into account the uncertainties in the n_e and T_e

Table 3. Reactions taken into account in the model for the neutral and charged oxygen species. The rate coefficients for the two- and three-body reactions are in $cm^3\ s^{-1}$ and $cm^6\ s^{-1}$, respectively, and the decay frequencies are in s^{-1}. $\sigma(\epsilon)$ denotes an electron impact cross section to be integrated with the calculated EEDF; the various $\sigma(\epsilon)$ were taken from [40, 49] and references therein.

	Processes	Rate coefficients	References
R25	$e + O_2(X, 0) \rightarrow e + O_2(a)$	$\sigma(\epsilon)$	
R26	$e + O_2(a) \rightarrow e + O_2(X,0)$	$\sigma(\epsilon)$	
R27	$e + O_2(X, 0) \rightarrow e + O_2(b)$	$\sigma(\epsilon)$	
R28	$e + O_2(b) \rightarrow e + O_2(X,0)$	$\sigma(\epsilon)$	
R29	$e + O_2(a) \rightarrow e + O_2(b)$	$\sigma(\epsilon)$	
R30	$e + O_2(b) \rightarrow e + O_2(a)$	$\sigma(\epsilon)$	
R31	$e + O_2(X, 0) \rightarrow e + O(^3P) + O(^3P)$	$\sigma(\epsilon)$	
R32	$e + O_2(a) \rightarrow e + O(^3P) + O(^3P)$	$\sigma(\epsilon)$	
R33	$e + O_2(b) \rightarrow e + O(^3P) + O(^3P)$	$\sigma(\epsilon)$	
R34	$e + O_3 \rightarrow e + O(^3P) + O_2(X, 0)$	$\sigma(\epsilon)$	
R35	$O(^3P) + O_2(X, 0) + O \rightarrow O_3 + O$	$2.1 \times 10^{-34} \times \exp(345/T)$	[40, 50]
R36	$e + O_2(X, 0) \rightarrow O^- + O(^3P)$	$\sigma(\epsilon)$	
R37	$e + O_2(a) \rightarrow O^- + O(^3P)$	$\sigma(\epsilon)$	
R38	$O^- + O_2(a) \rightarrow O_3 + e$	$0.75 \times 1.9 \times 10^{-10}$	[50, 51]
R39	$O_2(a) + O_2 \rightarrow O_2(X, 0) + O_2$	$2.2 \times 10^{-18} \times (T/300)^{0.8}$	[40, 52]
R40	$O_2(a) + O \rightarrow O_2(X, 0) + O$	7×10^{-17}	[40, 52]
R41	$O_2(b) + O \rightarrow O_2(X, 0) + O$	4×10^{-14}	[5]
R42	$O_2(b) + O \rightarrow O_2(a) + O$	4×10^{-14}	[5]
R43	$O_2 + O_2(X, 0) + O(^3P) \rightarrow O_3 + O_2$	$6.4 \times 10^{-35} \times \exp(663/T)$	[40, 50]
R44	$O_2(a) + O_3 \rightarrow O_2(X, 0) + O_2(X, 0) + O(^3P)$	$5.2 \times 10^{-11} \times \exp(-2840/T)$	[40, 50]
R45	$O_2(b) + O_3 \rightarrow O_2(X, 0) + O_2(X, 0) + O(^3P)$	1.5×10^{-11}	[40, 50]
R46	$O(^3P) + O_3 \rightarrow O_2(X, 0) + O_2(X, 0)$	$0.5 \times 1.8 \times 10^{-11} \times \exp(-2300/T)$	[50, 53]
R47	$O(^3P) + O_3 \rightarrow O_2(a) + O_2(X, 0)$	$0.33 \times 1.8 \times 10^{-11} \times \exp(-2300/T)$	[50, 53]
R48	$O(^3P) + O_3 \rightarrow O_2(b) + O_2(X, 0)$	$0.17 \times 1.8 \times 10^{-11} \times \exp(-2300/T)$	[50, 53]
R49	$O_2(a) + O_2(a) \rightarrow O_2(X, 0) + O_2(b)$	$1.81 \times 10^{-18} \times \exp(700/T) \times (T/300)^{3.8}$	[54, 55]
R50	$O(^3P) + O(^3P) + O_2 \rightarrow O_2 + O_2(X, 0)$	$0.5 \times 3.81 \times 10^{-30} \times \exp(-170/T)/T$	[50, 53]
R51	$O(^3P) + O(^3P) + O_2 \rightarrow O_2(a) + O_2$	$0.33 \times 3.81 \times 10^{-30} \times \exp(-170/T)/T$	[50, 53]
R52	$O(^3P) + O(^3P) + O_2 \rightarrow O_2(b) + O_2$	$0.17 \times 3.81 \times 10^{-30} \times \exp(-170/T)/T$	[50, 53]
R53	$O(^3P) + O(^3P) + O \rightarrow O_2(X, 0) + O$	$3.6 \times 10^{-32} \times (1/T)^{0.63}$	[55]
R54	$O(^3P) + O_2 + O_3 \rightarrow O_3 + O_3$	$1.66 \times 10^{-34} \times \exp(T/300)$	[10]
R55	$e + O_2(X, 0) \rightarrow e + O(^3P) + O(^1D)$	$\sigma(\epsilon)$	
R56	$e + O_2(a) \rightarrow e + O(^3P) + O(^1D)$	$\sigma(\epsilon)$	
R57	$e + O_2(b) \rightarrow e + O(^3P) + O(^1D)$	$\sigma(\epsilon)$	
R58	$e + O(^3P) \rightarrow e + O(^1D)$		
R59	$e + O(^1D) \rightarrow e + O(^3P)$		
R60	$O(^3P) + O(^1D) \rightarrow O(^3P) + O(^3P)$	8×10^{-12}	[50]
R61	$O(^1D) + O_2 \rightarrow O(^3P) + O_2$	$7 \times 10^{-12} \times \exp(67/T)$	[50]
R62	$O(^1D) + O_2(X) \rightarrow O(^3P) + O_2(a)$	1×10^{-12}	[50]
R63	$O(^1D) + O_2(X) \rightarrow O(^3P) + O_2(b)$	$2.56 \times 10^{-11} \times \exp(67/T)$	[50]
R64	$O(^1D) + O_3 \rightarrow O_2(X, 0) + O_2(X, 0)$	1.2×10^{-10}	[50]
R65	$O(^1D) + O_3 \rightarrow O_2(X, 0) + 2O(^3P)$	1.2×10^{-10}	[50]
R66	$e + O_2(X, 0) \rightarrow e + e + O_2^+$	$\sigma(\epsilon)$	
R67	$e + O_2(a) \rightarrow e + e + O_2^+$	$\sigma(\epsilon)$	
R68	$e + O_2^+ \rightarrow O(^3P) + O(^3P)$	$2 \times 10^{-7} \times (300/T_e)$	[52]
R69	$e + O_2^+ \rightarrow O(^3P) + O(^1D)$	$1.95 \times 10^{-7} \times (300/T_e)^{0.7}$	[50]
R70	$e + O(^3P) \rightarrow e + e + O^+$	$\sigma(\epsilon)$	
R71	$O^+ + O_2(X, 0) \rightarrow O_2^+ + O(^3P)$	$2 \times 10^{-11} \times (300/T)^{0.5}$	[50, 55]
R72	$O^+ + O_2(a) \rightarrow O_2^+ + O(^3P)$	$2 \times 10^{-11} \times (300/T)^{0.5}$	[50] [a]
R73	$O^+ + O_3 \rightarrow O_2^+ + O_2(X, 0)$	1×10^{-10}	[52]
R74	$O^+ + O^- \rightarrow O(^3P) + O(^3P)$	2.8×10^{-7}	[33]
R75	$O_2^+ + O^- \rightarrow O(^3P) + O_2(X, 0)$	$9.6 \times 10^{-8} \times (300/T)^{0.5}$	[50]
R76	$O(^3P) + \text{wall} \rightarrow 1/2O_2(X, 0)$		
R77	$O(^1D) + \text{wall} \rightarrow O(^3P)$		
R78	$O_2(a) + \text{wall} \rightarrow O_2(X, 0)$		
R79	$O_2(b) + \text{wall} \rightarrow O_2(X, 0)$		

[a] Temperature dependence assumed in this work.

measurements, also show a very satisfactory agreement with the experimental results.

Finally, one last comparison is made with the results from the post-discharge device of Mozetič *et al* [24]. Here, the atomic oxygen concentrations are measured in the post-discharge of a surface-wave Ar–O_2 microwave discharge generated in a 0.5 cm diameter quartz tube with 2.45 GHz frequency, for three different mixture compositions

Table 4. Binary diffusion coefficients at $p = 1$ Torr and $T = 273$ K, in units of cm^2s^{-1}.

	Diffusing in		
Species	Ar	O_2	O
$Ar(^3P_2)$	39.74	79.15	200.5
$Ar(^3P_0)$	27.78	79.15	200.5
$O_2(a,b)$	79.15	141.3	206.4
$O(^3P)$	200.5	206.4	—
$O(^1D)$	200.5	206.4	321.2

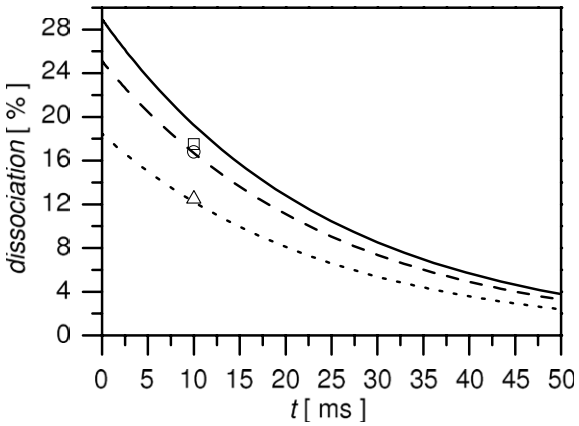

Figure 1. Oxygen dissociation degree in Ar–O_2: (——) and (□) at 2.14 Torr, 7% O_2; (– – –) and (○) at 2.22 Torr, 11% O_2; (· · · · · ·) and (△) at 2.54 Torr, 27% O_2. Lines represent our calculation results, and symbols the experimental data taken from [24].

as follows: (i) Ar–7%O_2 at 2.14 Torr (ii) Ar–11%O_2 at 2.22 Torr and (iii) Ar–27%O_2 at 2.54 Torr. Figure 1 shows the calculated dissociation degrees along the afterglow as a function of the species flight time in the afterglow, as well as the experimentally determined values. In the experimental system the afterglow tube that links the discharge with the post-discharge reactor is a 60 cm long tube of 2 cm diameter, the flight time of species through this tube at 1000 sccm is estimated to be about 10 ms. Taking into account the uncertainties in the estimation of the afterglow time where the experiments have been conducted, the calculated and experimentally determined dissociation degrees are in very good agreement, as shown in figure 1, which reinforces the validity of our kinetic model. A detailed analysis of the afterglow kinetics will be conducted elsewhere.

The comparisons with experiments conducted in this section have been performed for a relatively wide range of conditions. As a matter of fact, most discharge parameters varied, namely the field frequency, pressure, tube radius and mixture composition. The consistency of our calculations with the available experimental data for all these different conditions certifies the global validity of our description, allowing us to have a good degree of confidence in our results, to be explored in the rest of this paper.

3.2. Electron kinetics

We start our systematic study with the investigation of the electron kinetics in the Ar–O_2–O mixture. First of all we follow the evolution of the EEDF with the mixture composition.

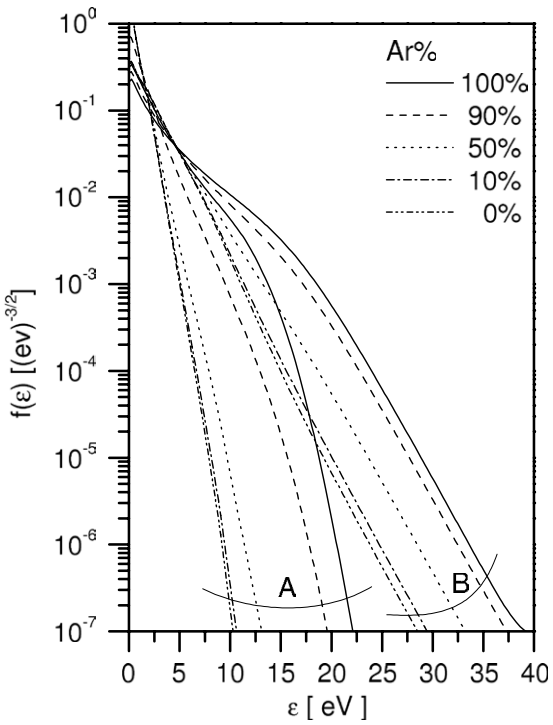

Figure 2. EEDF at 150 Td (A) and 550 Td (B) for different Ar–O_2 mixture compositions at 2 Torr with $[O]/[O_2] = 1$.

Figure 2 shows the EEDFs calculated for two values of the reduced electric field, $E/N = 15 \times 10^{-16}$ and 55×10^{-16} V cm^2—the former being representative of pure argon and the latter of pure oxygen at $p \sim 2$ Torr—and for four different mixture compositions. Note that these first results correspond only to the solution of the homogeneous Boltzmann equation at imposed electric field and not to the self-consistently determined discharge sustaining field (which are presented in figure 5). The same is true for the dissociation degree, which in the parametric calculations shown in figure 2 is kept constant at $[O(^3P)]/[O_2(X)] = 1$.

Among other information, these results allow us to understand how the discharge sustaining field changes with the mixture composition. Figure 2 shows that the addition of a relatively small content of oxygen into pure Ar can be enough to significantly alter the EEDF and, consequently, the electron ionization and excitation rate coefficients. The effect is especially remarkable at low values of the electric field. It can also be observed that the high-energy tails of the EEDFs are less populated as oxygen is added to the mixture, as a result of a higher global cross section in oxygen, as shown in figure 3. This explains why for constant electron density the discharge sustaining electric field should be higher near pure oxygen than near pure argon. It can also be noticed the very different shape of the EEDFs in pure Ar and in pure O_2. In very simple terms, this is a consequence of the fact that in pure oxygen the first energy loss is at about 0.2 eV, whereas in pure argon it occurs only at 11.5 eV, see figure 3. The 'barrier' at energies about 11 eV in pure argon is clearly seen in figure 2.

Let us now discuss the electron kinetics in an Ar–O_2 surface-wave microwave discharge as obtained from our self-consistent discharge model. Figure 4 presents the

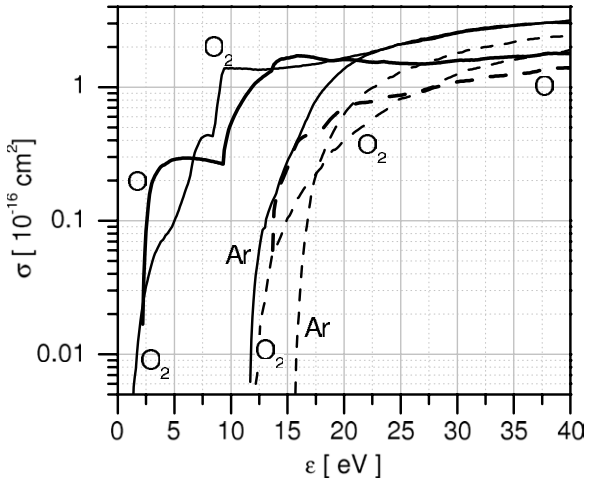

Figure 3. Total inelastic (——) and ionization (— — —) cross sections for Ar, O and O_2.

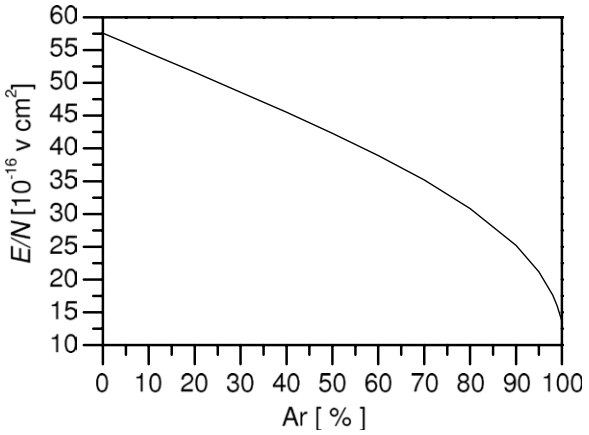

Figure 4. Reduced sustaining electric field, E/N, as a function of mixture composition.

self-consistently determined reduced sustaining electric field as a function of mixture composition, for $p = 2$ Torr and $n_e = 3.74 \times 10^{11}$ cm^{-3}. This figure confirms, as previously concluded in the analysis of figure 2, that the reduced electric field decreases continuously with the argon content in the mixture.

The corresponding self-consistent EEDFs are represented in figure 5 (cf as well figure 7). The high-energy tails of the EEDFs at energies above ≈20 eV clearly reflect the decrease in the sustaining field with Ar percentage. However, it is interesting to note that in the region close to the ionization thresholds of O_2 and Ar (≈12–16 eV) the EEDF is actually less populated the higher the oxygen fraction is, even if E/N is increasing. This is a consequence of the marked change in shape of the EEDF when oxygen is added into the mixture. As oxygen has a lower ionization threshold than Ar, a slightly less populated EEDF in oxygen at energies near the ionization threshold can result in the same total ionization rate. Since the electron density is not changing, the total ionization rate necessary to sustain the discharge should be about the same. However, in fact, the total ionization rate slightly increases with the percentage of O_2, as the total density of positive ions

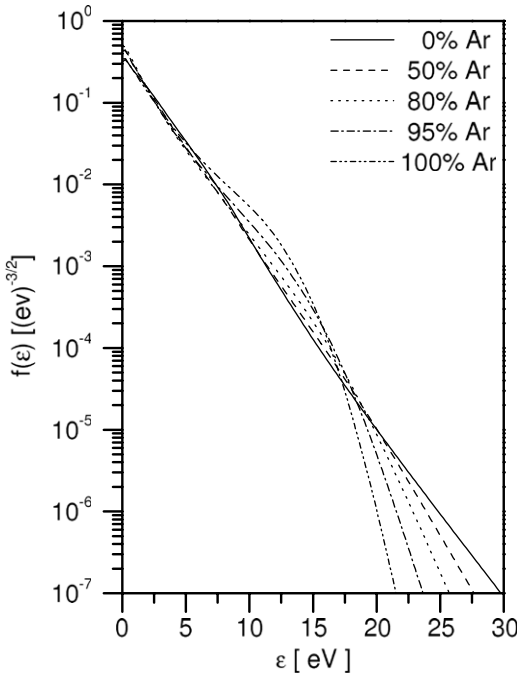

Figure 5. Self-consistent EEDFs calculated at $p = 2$ Torr, for different Ar contents in the mixture.

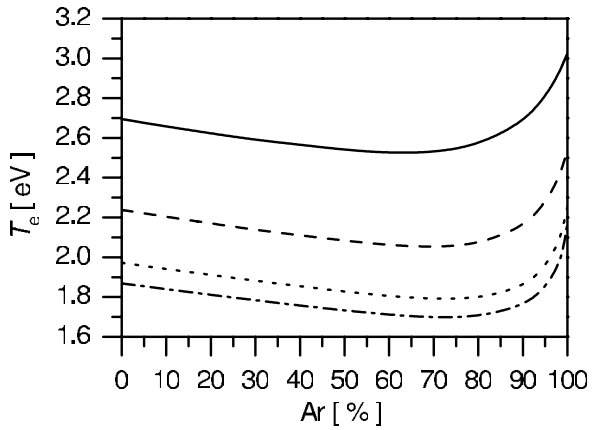

Figure 6. Electron kinetic temperature, $T_e = (2/3)\langle\varepsilon\rangle$, as a function of the mixture composition, for different values of pressure: 0.5 Torr (——), 1 Torr (— — —), 2 Torr (· · · · · ·), 3 Torr (— · —).

must balance the (constant) electron density and the increasing fraction of negative ions.

Finally, one last interesting effect occurs with the electron kinetic temperature, $T_e = (2/3)\langle\varepsilon\rangle$, as illustrated in figure 6. Due to the pronounced modifications in the EEDF with the addition of oxygen into argon, for low fractions of O_2 in the mixture T_e sharply decreases with O_2, in spite of the fact that E/N is increasing. Take note that T_e is representative of the electrons of the body of the distribution, and a zoom of the EEDFs in the region of energies $\varepsilon < 10$ eV, as depicted in figure 7, completely elucidates the phenomenon. Evidently, these effects are the outcome of a non-Maxwellian EEDF, demonstrating that a kinetic treatment of the electrons is mandatory in the system under investigation. In particular, popular fluid models where the electron excitation and ionization coefficients are obtained from values tabulated as

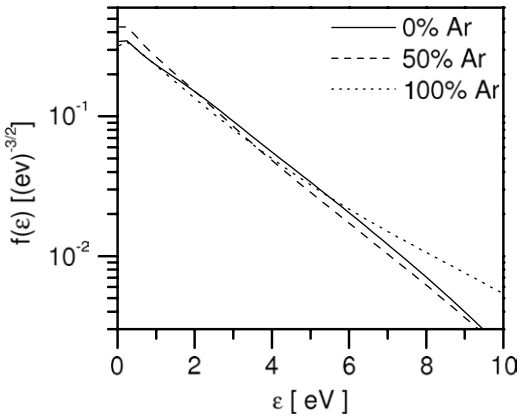

Figure 7. Zoom of figure 5 for $\varepsilon < 10$ eV.

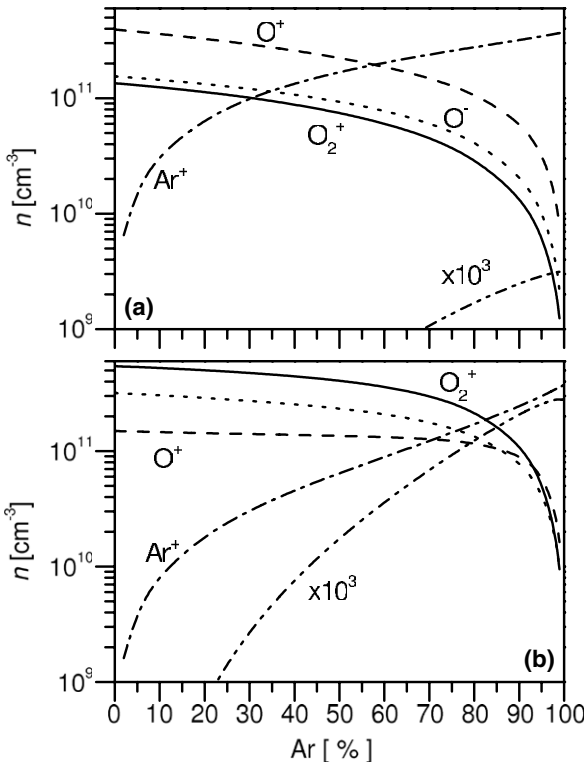

Figure 8. Density of ions as a function of the Ar percentage in the mixture at 0.5 Torr (*a*) and 2 Torr (*b*): O_2^+ (——), O^+ (— — —), O^- (· · · · · ·), Ar^+ (— · —) and Ar_2^+ (— · · —).

a function of the mean average energy are likely to introduce some errors.

3.3. Concentration of ions

As mentioned in the previous sections, the calculations are conducted for the critical electron density, $n_{ec} = 3.74 \times 10^{11}$ cm^{-3}, which does not change with the discharge operating conditions. Furthermore, the sustaining electric field is determined imposing that the total ionization rate must exactly balance the total electron loss rate, together with the quasi-neutrality condition.

Figure 8 shows the calculated densities of the different ions considered as a function of the Ar percentage in the mixture, for two values of the pressure, 0.5 and 2 Torr. As revealed by figure 8(*a*), the dominant ion at 0.5 Torr and in mixtures with up to 60% of Ar is O^+. However, Ar^+ becomes dominant at higher Ar content. Moreover, the concentrations of O^- and O_2^+ are comparable and within about a factor of 5 lower than the density of O^+. On the other hand, the density of Ar_2^+ is several orders of magnitude lower than the densities of the other ionic species. At the higher pressure of 2 Torr, figure 8(*b*) demonstrates that the Ar_2^+ density increases several orders of magnitude, although it is still negligible when compared with the population of Ar^+. Besides, at this pressure Ar^+ becomes the dominant ion only at the highest Ar content mixtures, i.e. for Ar percentages larger than about 85%. In contrast, for the lower Ar content mixtures the dominant ion is now O_2^+, while the density O^- is only a factor of 2 lower than that of O_2^+.

We start the analysis of the ion creation and loss mechanisms with the lower pressure case, $p = 0.5$ Torr.

For low Ar percentages, such as 20%, O_2^+ is created mostly by electron impact ionization of $O_2(X)$ (70%) and $O_2(a)$ (20%). Additional significant contributions come from the charge transfer processes between $O_2(X)$ and O^+ and Ar^+. At the same conditions the atomic ions, O^+ and Ar^+, are predominantly formed by electron impact ionization of the respective ground state atoms. In what concerns the negative ions, they are created by two processes with almost equal contribution, namely dissociative electron attachment of $O_2(X)$ (56%) and $O_2(a)$ (43%), respectively.

In the case of higher Ar content in the mixture, such as 90% Ar, an important role in the creation of Ar^+ is also played by electron impact stepwise ionization from the 4s states (about 12%, which can go up to 21% in pure argon), while the contribution of the charge transfer processes between $O_2(X)$ and Ar^+ to the creation of O_2^+ increases to 14%. As for O^-, the contribution of dissociative electron attachment of $O_2(a)$ to its creation decreases with Ar percentage.

In all conditions the positive ions are predominantly lost by ambipolar diffusion to the walls. In the case of a low Ar content mixture O^- is mostly destroyed by recombination with O^+ (60%). Other loss partners are $O_2(a)$ (21%) and Ar^+ (12%). At higher Ar percentages the role of $O_2(a)$ becomes negligible, O^- being mainly lost in ion–ion recombination with Ar^+ (80%).

As the pressure increases to 2 Torr, significant changes can be observed in the ion composition, O_2^+ gaining preponderance over O^+ and Ar^+. This is a consequence of the diminution of the dissociation degree (cf section 3.5), with the corresponding lower relative production of O^+ by direct electron impact and higher destruction of O^+ and Ar^+ through the charge transfer processes in collisions with O_2 resulting in O_2^+. This can be confirmed by looking at the creation mechanisms of O_2^+. In low Ar content mixtures, the contribution of charge transfer from O^+ increases from 6% to 22% with pressure. On the other extreme, at high Ar content, in particular for 90% Ar, the role of the charge transfer processes that involve Ar^+ ions increases with pressure, in the case of O_2^+ production from 14% to 45%, while in the case of O^+ from 2% to 15%. Another ionic species whose kinetics vary with pressure is the negative ion O^-. For low Ar percentages the principal creation process becomes

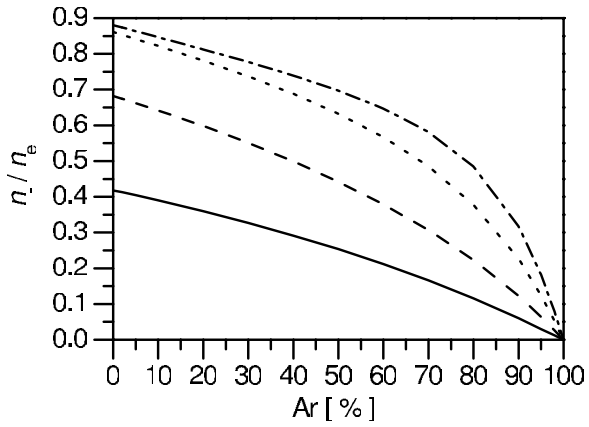

Figure 9. Electronegativity as a function of the mixture composition at different pressures: 0.5 Torr (——), 1 Torr (— — —), 2 Torr (· · · · · ·), 3 Torr (— · —).

dissociative electron attachment of $O_2(a)$ (55%), while O^- is now predominantly lost in detachment with $O_2(a)$ (80%).

As we have just seen the discharge contains a high density of O^- ions. Figure 9 shows the electronegativity parameter, $\alpha = n_-/n_e$, as a function of the Ar percentage in the mixture, for different values of pressure. The electronegativity increases with pressure, e.g. in pure O_2 from 0.4 at 0.5 Torr to 0.87 at 3 Torr. However, we should bear in mind that the electron density does not change with pressure. Moreover, the electronegativity decreases with the Ar percentage, as expected. A similar value of electronegativity, namely $\alpha = 0.6$, was found in an O_2 ICP discharge at 0.1 Torr at low power (100 W), with an electron density of 2×10^{10} cm^{-3}, by Gundmundsson *et al* [31].

3.4. Concentration of argon species

In this section we study the evolution of the densities of the argon neutral species with the mixture composition. The population of the four levels of the $3p^5 4s$ configuration, i.e. the two metastable $^3P_0$ and $^3P_2$ and the two resonant $^3P_1$ and $^1P_1$ states, is followed together with that of the $^1S_0$ ground state. The Ar atoms in resonant states give rise to VUV radiation in the 104–107 nm range, thus playing an important role in several applications, such as plasma sterilization [1, 14, 41, 65], light sources, as well as in the case of etching of polyolefins (hexatriacontane—HTC) [66]. Take note that the 4p states are taken into account in the model as well (cf table 1).

Figure 10 shows the densities of the Ar atoms in different states as a function of the mixture composition, for two values of pressure. The densities of ground and excited state atoms naturally decrease with O_2 addition into Ar. The same is true with the relative density of excited states, relative to that of ground state atoms. The decrease in the relative density of metastable and resonant state atoms is very sharp with a small O_2 addition. A similar effect has been observed by Rauf and Kushner in a CCP in the 0.1–1 Torr range [67]. However, this decrease becomes more moderate at about 30% O_2 in the case of 0.5 Torr and 15% O_2 at 2 Torr. In mixtures with oxygen percentages higher than 30%, the excited atoms densities at 0.5 Torr become about four orders of magnitude lower than

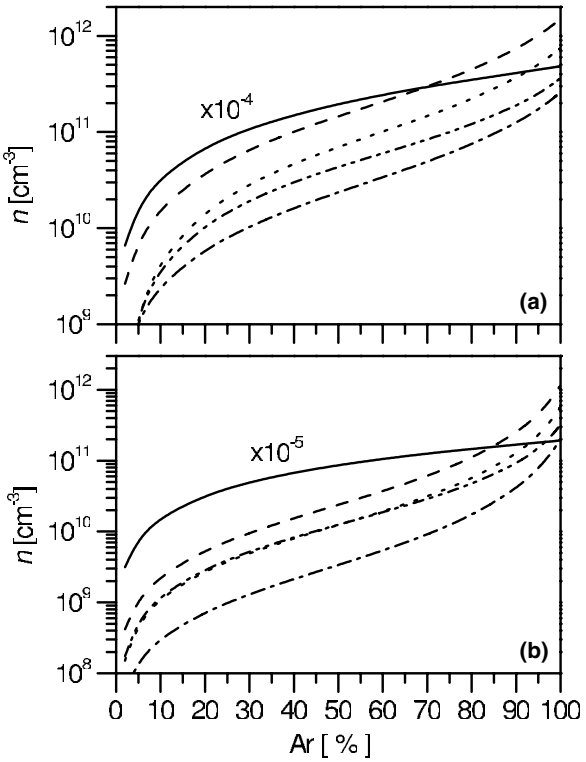

Figure 10. Density of the different Ar atomic states as a function of Ar percentage in the Ar–O_2 mixture, at 0.5 Torr (*a*) and at 2 Torr (*b*): Ar($^1S_0$) (——), Ar($^3P_2$) (— — —), Ar($^3P_1$)(· · · · · ·), Ar($^3P_0$) (— · —), Ar($^1P_1$) (— · · —).

that of ground state atoms, while at 2 Torr this difference is of five orders of magnitude. The most populated excited state is the Ar($^3P_2$) metastable, while the lowest concentration is obtained for the Ar($^3P_0$) metastable.

It is interesting to study the importance of the different processes in the population and depopulation of the metastable and resonant states. In pure Ar and at pressure $p = 0.5$ Torr, the Ar($^3P_2$) metastable is mostly created by electron excitation of the ground state Ar($^1S_0$) (30%), and through three further reactions which give similar contributions: electron deexcitation of the Ar($^3P_1$) (17%) and Ar($^3P_0$) (18%), and radiative deexcitation of the 4p states (25%). The electron deexcitation from the Ar($^1P_1$) resonant state contributes with about 8% to the Ar($^3P_2$) formation. The latter state is depopulated due to electron excitation to the resonant states (20–20%), to the $^3P_0$ metastable state (20%) and also to the 4p states (30%).

The Ar($^3P_0$) metastable is predominantly created by excitation from Ar($^3P_2$) (61%) and radiative deexciation of the 4p states (25%). Direct excitation from ground state Ar contributes with about 11% to Ar($^3P_0$) creation. This metastable is mostly depopulated through electron-induced deexcitation creating Ar($^3P_2$) metastable (54%) and excitation to the 4p states (39%).

The resonant states, Ar($^1P_1$) and Ar($^3P_1$), are formed by three processes giving almost equal contributions: (i) electron excitation from the ground state, (ii) stepwise excitation from the Ar($^3P_2$) metastable and (iii) radiative decay of the 4p states. The main loss channel of Ar($^1P_1$) is radiative deexcitation

(65%)—a very significant loss in the ensemble of the 4s states—, further important contributions are additionally given by the electron-induced deexcitation to $Ar(^3P_2)$ (11%), and excitation to the 4p states (20%). In the case of $Ar(^3P_1)$, the highest contribution to its destruction comes from the electron excitation to the 4p states, while the other two processes have an almost equal contribution of about 26%.

The analysis in the previous paragraphs reveals that the kinetics of all the 4s states are strongly coupled. Indeed, the total population of these states is essentially determined by their electron impact excitation from the ground state, $Ar(^1S_0)$, and by the direct excitation of the higher states with their ensuing radiative decay, on the side of creation, and by the radiative decay of the resonant states, from the side of destruction. The electron-induced processes among the 4s states, which appear as major source and loss terms in absolute values, essentially redistribute, very effectively, their relative populations. Nevertheless, they do not constitute actual losses from this group of states.

As pointed out earlier, with the addition of a small amount of oxygen a fast decrease in the excited atoms' relative density (relative to the ground state Ar atom) occurs. This is due to the strong quenching of these atoms by O_2 and $O(^3P)$, reactions (R15)–(R17). With 10% of O_2 in the mixture, these processes have a total contribution of about 2–4% to the depopulation of the 4s states. However, if we do not count the re-distribution among the 4s states as effective destruction mechanisms, the quenching by O_2 and O represents about 25% of the destruction of the 4s states. This number is significantly larger at $p = 2$ Torr, reaching a value higher than 60%. Evidently, with further oxygen addition the importance of these processes still increases and consequently the production and destruction pathways of excited state atoms change. At 90% of O_2 in the mixture, the dominant process for the creation of metastable and resonant states becomes the electron excitation from the ground state, with a contribution of about 70% to their sources. The exception is the $Ar(^3P_0)$ metastable, 46% being created by stepwise electron excitation from $Ar(^3P_2)$.

3.5. Concentration of oxygen species

In this section we turn our attention to the oxygen species present in an Ar–O_2 surface-wave microwave discharge. Figure 11 shows the density of the different oxygen species as a function of the Ar percentage in the Ar–O_2 mixture, for pressures of 0.5 and 2 Torr. At the lowest pressure investigated, $p = 0.5$ Torr, the dominant oxygen species is the $O(^3P)$ atom for any mixture composition, followed by the $O_2(X)$ molecule, see figure 11(*a*). The difference between the two densities increases from a factor of 2 to a factor of 4 with the Ar percentage. The density of excited $O(^1D)$ atoms is more than two orders of magnitude lower than that of the ground state atoms in the case of low Ar content mixtures. However, at mixtures with Ar percentages higher than 50% the density of $O(^1D)$ decreases slower than that of $O(^3P)$ with Ar percentage. Similar results have been obtained in a CCP at 0.1 Torr by Kitajima *et al* [2]. In what concerns the excited $O_2(a)$ and $O_2(b)$ molecules, their densities relative to the ground state $O_2(X)$ molecule decrease with the Ar percentage in the mixture, reaching densities one order of magnitude lower than that of $O_2(X)$ in mixtures with Ar percentage higher than 98% in the case of $O_2(a)$ and 80% in that of $O_2(b)$. Finally, the lowest density is the one of the O_3 molecule, whose density relative to the $O(^3P)$ density decreases from 10^{-4} to 10^{-6} with Ar percentage.

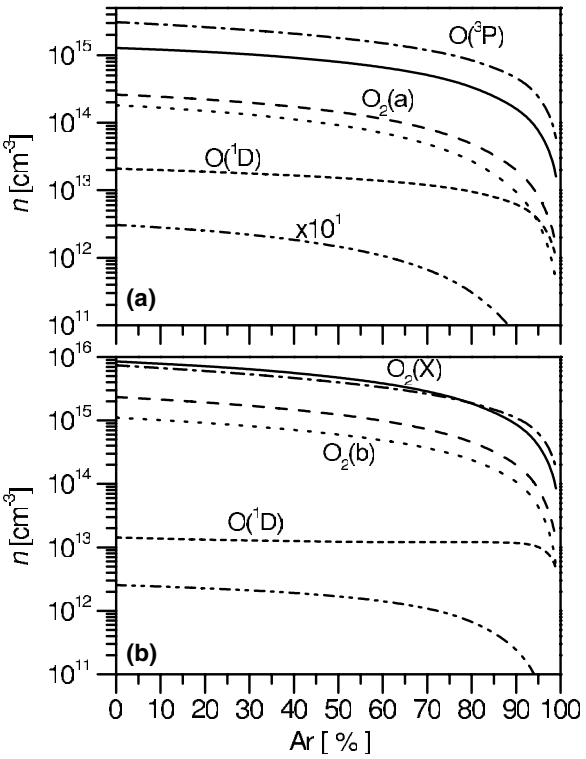

Figure 11. Density of the different oxygen species as a function of Ar percentage in the Ar–O_2 mixture, at 0.5 Torr (*a*) and at 2 Torr (*b*): $O_2(X)$ (——), $O_2(a)$ (— — —), $O_2(b)$ (· · · · · ·), $O(^3P)$ (— · —), $O(^1D)$ (– – –), O_3 (— · · —).

By increasing the pressure the $O_2(X)$ density, relative to that of $O(^3P)$, increases as well. As a result, at 2 Torr pressure $O_2(X)$ has become the dominant oxygen species in mixtures with Ar percentages lower than 80%, as revealed by figure 11(*b*). In what concerns the other oxygen species their densities show very similar behaviour to that observed at the lower pressure, with slight changes in their relative densities compared with the 0.5 Torr case.

One important characteristic of oxygen discharges is the dissociation degree of O_2 molecules. As we have just seen, under certain conditions $O(^3P)$ atoms can be the dominant species in the discharge, such as in the case of $p = 0.5$ Torr described in figure 11(*a*). Figure 12 depicts the dissociation degree ($[O(^3P)]/2[O_{2in}]$), $[O_{2in}]$ denoting the oxygen concentration entering the discharge, as a function of the Ar percentage in the mixture, at four different pressures. The highest dissociation degree is obtained at the lowest pressure, 0.5 Torr. This is a consequence of the decrease in the electron impact dissociation rates with pressure, related to the decrease in the electron kinetic temperature illustrated in figure 6. At constant pressure the dissociation degree shows a monotonic increase with the Ar content, as a result of the

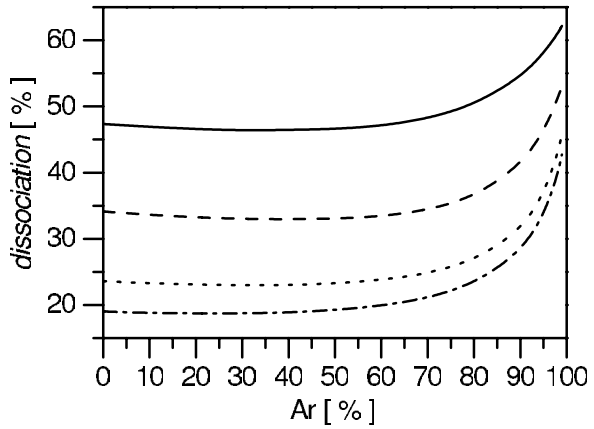

Figure 12. Dissociation degree as a function of the Ar percentage in the mixture for different values of pressure: 0.5 Torr (——), 1 Torr (— — —), 2 Torr (· · · · · ·), 3 Torr (— · —).

increasing importance of the Ar(4s) induced O_2 dissociation ((R15) and (R16)). These processes become important at the higher Ar percentages, the dissociation degree thus increasing with a higher rate at Ar percentages higher than about 80%.

In pure O_2, $O(^3P)$ is predominantly created by electron impact dissociation of $O_2(X)$, $O_2(a)$ and $O_2(b)$ ((R31)–(R33), (R55)). An addition of Ar into the mixture such as 50% does not influence considerably the role of the creation and destruction processes observed in pure O_2. The contribution of Ar(4s) induced O_2 dissociation ((R15) and (R16)) to the $O(^3P)$ creation is negligible at this condition, less than 2% for both pressures. However, with further Ar addition the importance of these processes increases and changes more remarkably the molecular kinetics. For instance, at 90% Ar in the mixture, the contribution of the Ar(4s) induced O_2 dissociation to the formation of $O(^3P)$ is nearly the same as electron impact dissociation of $O_2(X)$ (R31). The main loss processes of $O(^3P)$ are recombination at the wall and electron excitation to the ^1D state. Nevertheless, this latter process is in good part compensated by the deactivation processes of $O(^1D)$ that result in $O(^3P)$, such as wall deactivation (R77) and quenching by $O(^3P)$ (R60) and O_2 ((R61) and (R63)), thus wall recombination is the key destruction mechanism determining the final concentration of O atoms.

In what concerns excited $O(^1D)$ atoms, their kinetics is strongly correlated with the one of ground state $O(^3P)$ atoms. As a matter of fact, the former are predominantly created by electron impact excitation of the latter (R58), with a relative contribution of the order of ∼70%. The contribution of dissociation from the Ar(4s) states is essentially negligible, except for the higher percentages of Ar in the mixture. For instance, with 90% Ar in the mixture it still contributes only about 5% to the total creation of $O(^1D)$. On the other hand, $O(^1D)$ is destroyed by quenching to the ground state in collisions with $O(^3P)$ (R60), $O_2(X)$ ((R61)–(R63)), Ar (R22) and at the wall. Of particular importance is the quenching by O_2 leading to the formation of $O_2(b)$ molecules (R63). As the rate of reaction (R22) with Ar is lower than the rates of the reactions involving O_2, the total quenching due to gas-phase collisions decreases with Ar addition, making wall deactivation more important in these conditions and justifying the quite flat profile of $O(^1D)$ with the Ar content. Evidently, the contribution of the latter process is higher at the lower pressures (52% and 6% in pure O_2 at $p = 0.5$ and 2 Torr, respectively, and 82% and 29% for the same pressures and a mixture with 90% of Ar).

The kinetics of the O_2 excited states is strongly coupled, as the electron impact processes involving transitions among the group of states $O_2(X, a, b)$ are very significant. $O_2(a)$ is mainly populated by electron impact collisions with $O_2(X)$ (R25) and $O_2(b)$ (R30), their relative importance depending on pressure and mixture composition. For the conditions investigated, the joint contribution of these two reactions to the total production of $O_2(a)$ molecules is always larger than 85%. Other minor contributions are given by the quenching of $O(^1D)$ by $O_2(X)$ (R63) and $O_2(b)$ by O atoms (R42). The role of the latter reaction can be important near pure oxygen and at the higher pressures, reaching 9.4% in pure O_2 at 2 Torr. The metastable state $O_2(a)$ is destroyed also by electron impact, in collisions leading to the formation of $O_2(X)$, $O_2(b)$ and to dissociation. It is worth emphasizing that the destruction mechanism forming two oxygen atoms, which accounts for about 50% of the total destruction of $O_2(a)$ at 0.5 Torr and 30–40% at 2 Torr, further couples the kinetics of the molecular metastables to the atomic kinetics, and forms an effective removal channel of the ensemble of molecular excited states.

As for the second metastable state, $O_2(b)$, it is formed by electron impact on $O_2(X)$ (R27) and $O_2(a)$ (R29), as well as by the important quenching of $O(^1D)$ with O_2 (R63). This last process is dominant in the creation of $O_2(b)$ for a broad range of conditions (it accounts for 75% and 66% of the total creation of $O_2(b)$ in pure oxygen at 0.5 Torr and 2 Torr, respectively, and 55% and 68% for a mixture containing 90% of Ar, for the same pressures). From the side of destruction, the most important mechanisms are electron impact collisions forming $O_2(a)$ and leading to dissociation, and the quenching at the wall. A minor contribution is given by electron superelastic collisions to the ground state (R28), whereas the quenching with O atoms ((R41) and (R42)) becomes somewhat important at higher pressures and mixtures with high oxygen content (contributes 13% in pure O_2 and at $p = 2$ Torr).

Finally, O_3 is created in the discharge due to the recombination of O^- with $O_2(a)$ (R38), for all conditions under study. It is lost through electron dissociation (R34) and dissociation induced by $O(^3P)$ ((R46)–(R48)), $O(^1D)$ ((R64) and (R65)), $O_2(b)$ (R45) and $O_2(a)$ (R44). However, the relevance of the different destruction processes changes considerably with the mixture composition and pressure. For instance, at $p = 0.5$ Torr and 90% Ar in the mixture, electron dissociation is the dominant process (66%), while the contribution of dissociation in collisions with $O(^1D)$ is 20% and the one of collisions with $O_2(b)$ a mere 2%. These numbers are modified to 25%, 26% and 15%, respectively, in pure oxygen at the same pressure, and to 20%, 30% and 20% at 2 Torr in mixture with 90% Ar. At the higher pressure and high oxygen content, destruction in collisions with $O_2(b)$ becomes the dominant O_3 destruction mechanism.

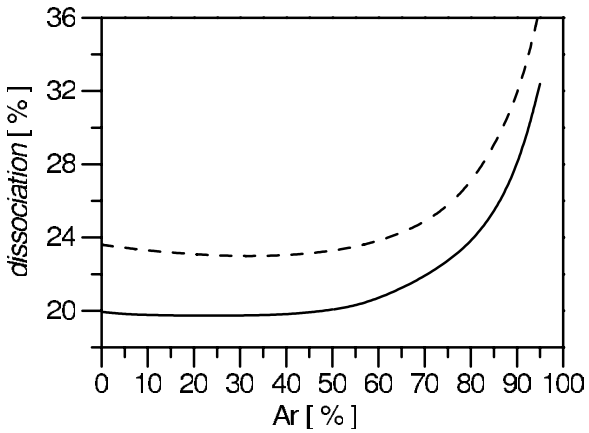

Figure 13. Dissociation degree for two different tube radii: 0.25 cm (——) and 0.5 cm (— — —), at 2 Torr.

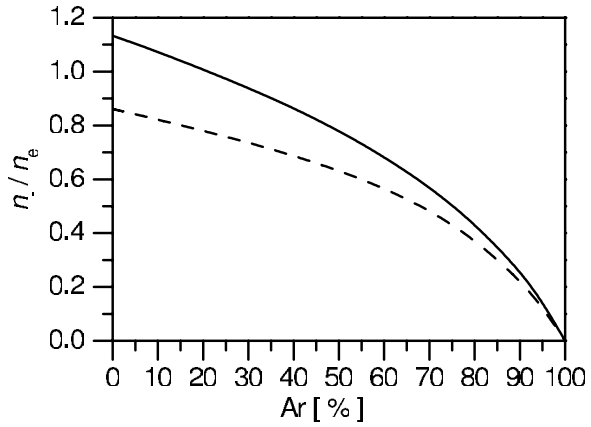

Figure 14. Electronegativity for two different tube radii: 0.25 cm (——) and 0.5 cm (— — —), at 2 Torr.

3.6. Effect of the discharge tube radius and atomic surface recombination

As shown in the previous section, oxygen atoms are primarily lost due to their recombination on the discharge tube walls. Therefore, it is expected that the size of the tube radius can have a significant influence on the density of atoms in the discharge. On the other hand, ions and electrons also predominantly recombine on the walls and, as is well known, because of this in a lower diameter tube a higher electric field is needed in order to sustain a quasi-neutral plasma with the same electron density. Evidently, the variation of the sustaining field influences all the electron impact processes, including dissociation. That being so, these two effects have an impact on dissociation in opposite directions. Indeed, when the tube radius is increased the atomic losses are smaller, leading to an increase in the dissociation degree, whereas the lower electric field tends to reduce the dissociation degree.

Figure 13 presents the dissociation degree for two different tube radii as a function of the mixture composition. The changes occurring in the dissociation degree are due to the competition between the two different effects just mentioned. According to the calculations, the atomic concentration is higher for the larger diameter tube, so that the direct influence of atomic recombination is the dominant effect. Besides, the profiles of the dissociation degree with Ar are very similar when the tube radius changes, showing that the overall influence of Ar on the dissociation kinetics is quite independent of the tube radius.

The modification of the ion loss rates due to the variation of the discharge tube radius influences the charge composition of the plasma, since negative ions, which recombine only in the gas phase, are also present. Figure 14 shows the electronegativity as a function of mixture composition for two different tube radius values. The results show that the density of negative ions is higher in the smaller diameter tube. According to the calculations, the reduction in the negative ions is due to the decrease in the rate of O^- creation through electron dissociative attachment of $O_2(X)$ with the tube radius.

Finally, the importance of surface recombination of atoms can also be altered if the recombination probability changes.

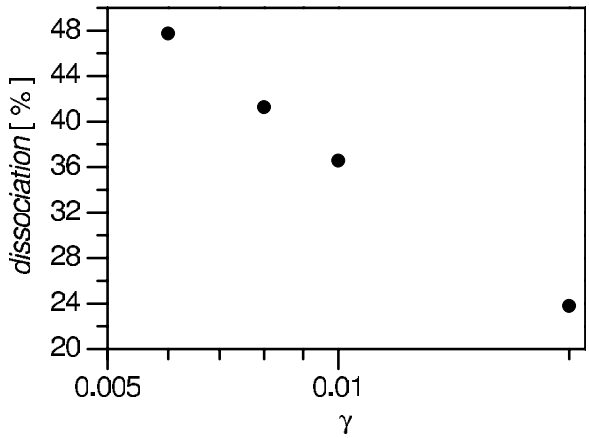

Figure 15. Dissociation degree as a function of the recombination probability for the 0.5 cm radius tube, in a 95%Ar–5%O_2 discharge at 2 Torr.

Therefore, we investigate additionally the effect of the value of surface recombination probability of atoms on the atomic density. For a given material, the heterogeneous recombination depends on the state of the surface as well as on the surface temperature. In the case of surfatron generated surface-wave discharges, wall temperatures higher than 400 K are often achieved, depending on the effectiveness of the cooling (forced air or water cooling) applied through the surfatron body. Here, we study the influence on the O-atoms density of the surface recombination probability, γ, as the surface temperature varies in the range 400–500 K. The values of γ are taken from Macko *et al* [56], who have shown (figure 15 from [56]) that γ increases sharply with the wall temperature in this region, by more than a factor of 3. Figure 15 shows the dissociation degree for several values of γ. In the temperature range considered, the increase in the recombination probability induces a decrease in dissociation degree by a factor of 2, demonstrating the importance of an accurate treatment of the heterogeneous processes.

4. Conclusions

In this work we have developed a kinetic model to study low pressure surface-wave Ar–O_2 discharges. The working

conditions were chosen to be close to those found in the plasma sterilization [1, 21] and polymer treatment studies [3], namely a surface-wave plasma generated at 2.45 GHz in a 1 cm diameter quartz tube, operating at pressures in the range 0.5–3 Torr. The model was validated from the comparison of the calculations with available experimental data both for the electron and the heavy-particle kinetics. The very good agreement between the model predictions and the experimental results, for a diversified range of conditions, substantiates the correctness of our description.

It was shown that the EEDF is strongly non-Maxwellian, its shape changing markedly when O_2 is added into an Ar discharge. Therefore, a kinetic description is necessary and analyses based on electron average energies must be handled with extreme care. For instance, although the reduced electric field sustaining the discharge continuously decreases with the Ar content in the mixture, the modifications in the shape of the EEDF lead to a minimum of the electron temperature for Ar percentages around 80%.

It was further concluded that the ion composition changes with pressure. Except for discharges near pure argon, where Ar^+ is the dominant positive ion, O^+ is the major positive ion at the lower pressures, O_2^+ becoming predominant at the higher pressures. Besides, negative O^- ions are largely present in the discharge. The electronegativity of the discharge can exceed one, and accordingly, any accurate calculation of the electric field has to take the effects of negative ions into account.

Oxygen is strongly dissociated, the dissociation degree reaching values as high as 60%, as a result of electron impact collisions with ground state and metastable O_2 molecules, as well as in heavy-particle collisions of O_2 with the Ar(4s) states. The latter mechanisms contribute to making the dissociation degree larger in mixtures containing large amounts of Ar than at low Ar content. The substantial dissociation degree observed indicates that the relative concentration of oxygen species also changes with pressure, oxygen atoms being the most populated species at the lower pressures and ground state $O_2(X)$ molecules at higher pressures.

The kinetics of the Ar(4s) states is strongly coupled, as the electron inelastic and superelastic collisions among these states are very effective. Together with the stepwise excitation of the (4p) levels with their subsequent decay back to (4s), they efficiently redistribute the total population of these states. A major loss of the ensemble of the Ar(4s) states is due to the radiative decay of the $Ar(^1P_1)$ resonant state.

A quite similar situation takes place with $O_2(a, b)$ and $O(^3P, ^1D)$. Electron impact reactions among these states are very significant, including dissociation from the molecular metastable states $a\,^1\Delta_g$ and $b\,^1\Sigma_g^+$. An important gas-phase reaction among heavy-particles is the quenching of $O(^1D)$ by $O_2(X)$ leading to the formation of $O_2(b)$, $O(^1D) + O_2(X) \rightarrow O(^3P) + O_2(b)$, which, in addition to electron impact processes, ensures a strong coupling between the atomic and molecular oxygen kinetics.

The role of surface processes is very important, affecting the overall kinetics of the discharge. Therefore, the influence of the tube radius and the atomic recombination probability at the wall has also been investigated. It is verified that the dissociation degree increases with the discharge tube radius, while it decreases with the atomic surface recombination of O atoms. An optimization of atomic oxygen production can then be achieved by a careful choice of the wall material and temperature, which directly affect the recombination probability, and the tube dimensions. These characteristics may have a significant influence on the degree of homogeneity of O atoms on sterilization afterglow reactors, for instance, as previously pointed out in [68] for the case of N_2–O_2.

Work is in progress to extend our investigation to the early and remote afterglow regions, as well as to the study of the very promising ternary mixture Ar–O_2–N_2. This mixture has all the advantages of Ar–O_2 mixtures and provides additionally the strong UV radiation from the NO(A) and NO(B) molecules.

Acknowledgments

The work has been supported by the Hungarian Science Foundation OTKA, through project F-67556 and by Janos Bolyai Research Scholarship of the Hungarian Academy of Sciences. The authors want to express their gratitude to Drs Jorge Loureiro and Thierry Belmonte, for very rewarding discussions.

References

[1] Moreau S, Moisan M, Tabrizian M, Barbeau J, Pelletier J, Ricard A and Yahia L H 2000 *J. Appl. Phys.* **88** 1166
[2] Kitajima T, Nakano T and Makabe T 2006 *Appl. Phys. Lett.* **88** 091501
[3] Mafra M, Belmonte T, Poncin-Epaillard F, Maliska A and Cvelbar U 2009 *Plasma Process. Polym.* **6** S198
[4] Rawlins W T, Lee S, Kessler W J and Davis S J 2005 *Appl. Phys. Lett.* **86** 051105
[5] Ionin A A, Kochetov I V, Napartovich A P and Yuryshev N N 2007 *J. Phys. D: Appl. Phys.* **40** R25
[6] Bauville G, Lacour B, Magne L, Puech V, Boeuf J P, Muñoz-Serrano E and Pitchford L C 2007 *Appl. Phys. Lett.* **90** 031501
[7] Santos Sousa J, Bauville G, Lacour B, Puech V, Touzeau M and Pitchford L 2008 *Appl. Phys. Lett.* **93** 011502
[8] Raballand V, Benedikt J, Wunderlich J and von Keudell A 2008 *J. Phys. D: Appl. Phys.* **41** 115207
[9] Yasuda Y, Zaima S, Kaida T and Koide Y 1990 *J. Appl. Phys.* **67** 2603
[10] Belmonte T, Czerwiec T, Gavillet J and Michel H 1997 *Surface Coat. Technol.* **97** 642
[11] Drenik A, Cvelbar U, Ostrikov K and Mozetič M 2008 *J. Phys. D: Appl. Phys.* **41** 115201
[12] Nagatsu M, Terashita F, Nonaka H, Xu L, Nagata T and Koide Y 2005 *Appl. Phys. Lett.* **86** 211502
[13] Vujoševic D, Mozetič M, Cvelbar U, Krstulović N and Miloševic S 2007 *J. Appl. Phys.* **101** 103305
[14] Halfmann H, Denis B, Bibinov N, Wunderlich J and Awakowicz P 2007 *J. Phys. D: Appl. Phys.* **40** 5907
[15] Kylián O and Rossi F 2009 *J. Phys. D: Appl. Phys.* **42** 085207
[16] Balazs D J, Triandafillu K, Wood P, Chevolot Y, van Delden C, Harms H, Hollenstein C and Mathieu H J 2004 *Biomaterials* **25** 2139
[17] Amanatides E, Mataras D, Katsikogianni M and Missirlis Y F 2006 *Surf. Coat. Technol.* **200** 6331
[18] Mafra M, Belmonte T, Maliska A, da Silva Sobrinho A S, Cvelbar U and Poncin-Epaillard F 2008 *Key Eng. Mater.* **373–374** 421

[19] Ricard A, Gaillard M, Monna V, Vesel A and Mozetič M 2001 *Surf. Coat. Technol.* **142–144** 333
[20] Ricard A and Monna V 2002 *Plasma Sources Sci. Technol.* **11** A150
[21] Ricard A, Monna M and Mozetič M 2003 *Surf. Coat. Technol.* **174–175** 905
[22] Czerwiec T, Gavillet J, Belmonte T, Michel H and Ricard A 1998 *Surf. Coat. Technol.* **98** 1411
[23] Mozetič M, Ricard A, Babič D, Poberaj I, Levaton J, Monna V and Cvelbar U 2003 *J. Vac. Sci. Technol.* A **21** 369
[24] Mozetič M, Vesel A, Cvelbar U and Ricard A 2006 *Plasma Chem. Plasma Process.* **26** 103
[25] Granier A, Pasquiers S, Boisse-Laporte C, Darchicourt R, Leprince P and Marec J 1989 *J. Phys. D: Appl. Phys.* **22** 1487
[26] Pinheiro M J, Gousset G, Granier A and Ferreira C M 1998 *Plasma Sources Sci. Technol.* **7** 524
[27] Pinheiro M J, Gordiets B F and Ferreira C M 1999 *Plasma Sources Sci. Technol.* **8** 31
[28] Tristant P, Gousset G, Régnier C and Desmaison J 2002 *Plasma Sources Sci. Technol.* **11** 241
[29] Sá P, Loureiro J and Ferreira C M 1992 *J. Phys. D: Appl. Phys.* **25** 960
[30] Sá P, Loureiro J and Ferreira C M 1994 *J. Phys. D: Appl. Phys.* **27** 1171
[31] Gudmundsson J T, Kouznetsov I G, Patel K K and Lieberman M A 2001 *J. Phys. D: Appl. Phys.* **34** 1100
[32] Gudmundsson J T and Thorsteinsson E G 2007 *Plasma Sources Sci. Technol.* **16** 399
[33] Sato T and Makabe T 2008 *J. Phys. D: Appl. Phys.* **41** 035211
[34] Hayashi Y, Hirao S, Zhang Y, Gans T, O'Connell D, Petrović Z Lj and Makabe T 2009 *J. Phys. D: Appl. Phys.* **42** 145206
[35] Mérel P, Tabbal M, Chaker M, Moisan M and Ricard A 1998 *Plasma Sources Sci. Technol.* **7** 550
[36] Boisse-Laporte C, Chave-Normand C and Marec J 1997 *Plasma Sources Sci. Technol.* **6** 70
[37] Guerra V, Tatarova E, Dias F M and Ferreira C M 2002 *J. Appl. Phys.* **91** 2648
[38] Ferreira C M and Loureiro J 2000 *Plasma Sources Sci. Technol.* **9** 528
[39] Ferreira C M and Loureiro J 1989 *J. Phys. D: Appl. Phys.* **22** 76
[40] Guerra V and Loureiro J 1999 *Plasma Sources Sci. Technol.* **8** 110
[41] Philip N, Saoudi B, Crevier M-C, Moisan M, Barbeau J and Pelletier J 2002 *IEEE Trans. Plasma Sci.* **30** 1429
[42] Ferreira C M, Loureiro J and Ricard A 1985 *J. Appl. Phys.* **57** 82
[43] Ferreira C M and Loureiro J 1983 *J. Phys. D: Appl. Phys.* **16** 1611
[44] Piper L G, Velazco J E and Setser D W 1973 *J. Chem. Phys.* **59** 3323
[45] Balamuta J and Golde M F 1982 *J. Phys. Chem.* **86** 2765
[46] Olsen R E, Peterson J R and Moseley J 1970 *J. Chem. Phys.* **53** 3391
[47] Borrell P M, Borrell P, Grant K R and Pedley M D 1982 *J. Phys. Chem.* **86** 700
[48] Midey A J and Viggiano A A 1998 *J. Chem. Phys.* **109** 5257
[49] Gousset G, Pinheiro M, Sá P A, Touzeau M, Vialle M and Loureiro J 1991 *J. Phys. D: Appl. Phys.* **24** 290
[50] Eliasson B and Kogelschatz U 1986 *Brown Boveri Forschungszentrum Report KLR 86-11 C*
[51] Belostotsky S B, Economou D J, Lopaev D V and Rakhimova T V 2005 *Plasma Sources Sci. Technol.* **14** 532
[52] Kossyi I A, Kostinsky A Yu, Matveyev A A and Silakov V P 1992 *Plasma Sources Sci. Technol.* **1** 207
[53] Feoktistov V A, Mukhovatova A V, Popov A M and Rakhimova T V 1995 *J. Phys. D: Appl. Phys.* **28** 1346
[54] Heidner III R F, Gardner C E, El-Sayed T M, Segal J I and Kasper J V V 1981 *J. Chem. Phys.* **74** 5618
[55] Gordiets B, Ferreira C M, Guerra V, Loureiro J, Nahorny J, Pagnon D, Touzeau M and Vialle M 1995 *IEEE TRans. Plasma Sci.* **23** 750
[56] Macko P, Veis P and Cernogora G S 2004 *Plasma Sources Sci. Technol.* **13** 251
[57] Rohlena K and Mašek K 1985 *Acta Phys. Slovaca* **35** 141
[58] Loureiro J 1991 *Chem. Phys.* **157** 157
[59] Cheng T S, Wu C Y, Chen C P, Li Y H, Chao Y C, Yuan T and Leu T S 2006 *Combust. Flame* **146** 268
[60] Hirschfelder J O, Curtiss C F and Bird R B 1964 *Molecular Theory of Gases and Liquids* (New York: Wiley)
[61] Tachibana K and Phelps A V 1981 *J. Chem. Phys.* **75** 3315
[62] Lawton S A and Phelps A V 1978 *J. Chem. Phys.* **69** 1055
[63] Muñoz A G 2007 *Planet. Space Sci.* **55** 1414
[64] de Vries N, Palomares J M, van Harskamp W J, Iordanova E I, Kroesen G M W and van der Mullen J J A M 2008 *J. Phys. D: Appl. Phys.* **41** 105209
[65] Pollak J, Moisan M, Kéroack D, Boudam M K 2008 *J. Phys. D: Appl. Phys.* **41** 135212
[66] Belmonte T, Pintassilgo C D, Czerwiec T, Henrion G, Hody V, Thiebaut J M and Loureiro J 2005 *Surf. Coat. Technol.* **200** 26
[67] Rauf S and Kushner M J 1997 *J. Appl. Phys.* **82** 2805
[68] Kutasi K and Loureiro J 2007 *J. Phys. D: Appl. Phys.* **40** 5612